

A S-type 2D/2D heterojunction via intercalating ultrathin g-C₃N₄ into NH₄V₄O₁₀ nanosheets and the boosted removal of ciprofloxacin

Yuxuan Ma ^a, Dan He ^b, Quansheng Liu ^c, Shukun Le ^{b,c}, Xiaojing Wang ^{a,b,*}

^a School of Ecology and Environment Department, Inner Mongolia University, Hohhot, Inner Mongolia, PR China

^b Inner Mongolia Key Laboratory of Chemistry and Physics of Rare Earth Materials, School of Chemistry and Chemical Engineering, Inner Mongolia University, Hohhot, Inner Mongolia, PR China

^c Inner Mongolia Key Laboratory of High-Value Functional Utilization of Low Rank Carbon Resources, Chemical Engineering College, Inner Mongolia University of Technology, Hohhot, Inner Mongolia, PR China



ARTICLE INFO

Keywords:
2D/2D g-C₃N₄/NH₄V₄O₁₀ heterojunction
Ultrathin g-C₃N₄ nanosheets
Photodegradation
Ciprofloxacin
Fluoride-containing organic pollutants

ABSTRACT

Exploring cheap, eco-friendliness, and highly efficiency photocatalysts for improving the degradation performance of ciprofloxacin (CIP) is a challenge in the environmental remediation field. Herein, 2D/2D ultrathin g-C₃N₄/NH₄V₄O₁₀ (CNNS/NH₄V₄O₁₀) heterojunction is successfully prepared by intercalating g-C₃N₄ nanosheets into the ultrathin NH₄V₄O₁₀ nanobelts. For the optimized 50-CNNS/NH₄V₄O₁₀, the removal rate is 92% for 10 mg·L⁻¹ CIP under simulated solar light, far better than the separated components CNNS and NH₄V₄O₁₀. Moreover, the wide degraded concentration of CIP ranges from 5 to 40 mg·L⁻¹ devotes a prospect of practical application. The mechanism investigation confirms the intercalating action can break the interlaminar bonding linkage of NH₄, which increases the surface NH₄⁺ content and promotes the steered adsorption capacity toward ciprofloxacin through binding to F⁻ in CIP via H-bonding. This work provides a novel design idea for constructing 2D/2D intercalated nanocomposite for the application in the removal of the deleterious fluoride-containing organic pollutants in water environment.

1. Introduction

Fluoroquinolones, a class of fluorine-containing drugs with a nitrogen miscellaneous double-ring as the basic skeleton, possess wide antibacterial spectrum, strong antibacterial activity, and small toxic side effects, being now commonly used in humans, animal husbandry and aquaculture industries [1]. However, the long-term consumption of fluoroquinolones leads to their quickly accumulation in food and environment, which constitutes a huge harm to human health and the ecological environment system. Therefore, the decontamination of quinolone residues is of increasing concern. As a typical represent of fluoroquinolones, Ciprofloxacin (CIP) is a kind of amphiphilic molecule, and it can stably exist in acidic or alkaline environment in different ion forms [2]. In the light of their extremely low volatility and high solubility in an aqueous environment, the residual of CIP in aqueous environment becomes more difficult to be removed. Many researches on the purify of CIP residues have been reported, such as biodegradation, adsorption, Fenton treatment, membrane separation, ozonation and photocatalytic treatment [3–6]. Among these approaches, the

adsorption-photocatalytic treatment technology is particularly prominent in consideration of its simple operation, no secondary pollution, and availability on the liquefiable contaminant [7]. Nevertheless, the high adsorption efficiency and completely smashed pollutant structure are still necessarily required for the photocatalytic materials applied in the decontamination of CIP residues in view of the industrial cost and environmental risk.

NH₄V₄O₁₀ is a typical laminar structure constructed by vanadium oxide polyhedral, in which the NH₄⁺ ions are interstratified at the layers of vanadium oxides. Due to the diversity and flexibility of its valence state and structure, NH₄V₄O₁₀ has received extensive attention in the electrochemical field, such as high-energy lithium batteries [8], chemical sensors/actuators [9] and electrochemical devices [10]. What's more, NH₄V₄O₁₀ has generally been applied as the excellent photocatalyst due to its excellent oxidation ability, quickly electrical conductivity, small band energy gap, and abundant active sites [10–13]. Withal, the ultrathin 2D structure and the affluent surface amino groups of the laminar NH₄V₄O₁₀ may dedicate to the strong adsorption of special fluorine contaminants, leading to a further effective

* Corresponding author at: School of Ecology and Environment Department, Inner Mongolia University, Hohhot, Inner Mongolia, PR China.
E-mail address: 12268145@qq.com (X. Wang).

photo-degradation after enrichment [14]. However, although these merits from ultrathin $\text{NH}_4\text{V}_4\text{O}_{10}$, it still need to be carefully concerned that the very short migrated path of the photo-generated carriers in these ultrathin materials will cause the quickly recombination. Meanwhile, the ultrathin nanosheets are easy to stack in virtue of the strong π - π bond energy, and thus reduce the active sites and ions diffuse. All gives a decayed photocatalytic activity and stability. To address these issues, constructing a heterojunction with the appropriate level alignment is expected a good strategy. As it knows, $\text{NH}_4\text{V}_4\text{O}_{10}$ is strong oxidative semiconductor with a big positive potential. If it is matched with a strong reduced semiconductor which possesses high negative potential to construct a S-type heterojunction, the photo-excited electrons from the upper band of oxidative semiconductor will be smoothly recombined with the holes from the lower band of the reduced one, leaving the high negative potential electrons and the very positive holes. Therefore, such an architecture can not only greatly improve the transfer and separation of photo-generated charges at the interface of the heterojunction but also well maintain the strong oxidative ability [15,16].

Graphitic carbon nitride ($\text{g-C}_3\text{N}_4$) belongs to the members of the 2D organic nanomaterials family and has applications in various fields, including in the fields of energy conversion, light-emitting devices, coatings and photocatalysis [17]. Specially, the very excellent stability and wide solar light absorption makes it a variety of applications in the photocatalytic degradation of organic pollutants and CO_2 reduction [18,19]. Nevertheless, the general shortcoming of laminated materials such as the instability and the carriers' quick recombination are ascribed to $\text{g-C}_3\text{N}_4$, which largely limit its photocatalytic application. There, it is generally as one of the participants to build a composite in order to achieve the enhanced photocatalytic activity, such as $\text{g-C}_3\text{N}_4/\text{CeO}_2$ [20], $\text{g-C}_3\text{N}_4/\text{Bi}_2\text{O}_2\text{CO}_3$ [21], $\text{g-C}_3\text{N}_4/\text{CdS}$ [22], $\text{g-C}_3\text{N}_4/\text{Bi}_2\text{S}_3$ [23], $\text{g-C}_3\text{N}_4/\text{ZIF-8}$ [24], $\text{g-C}_3\text{N}_4/\text{WO}_3$ [25]. Withal, $\text{g-C}_3\text{N}_4$ is a typical reduction-type semiconductor, thus it is expected that by assembling $\text{g-C}_3\text{N}_4$ with $\text{NH}_4\text{V}_4\text{O}_{10}$, a S-type heterojunction integrated the separated components merits will be formed [26]. In this architecture, $\text{g-C}_3\text{N}_4$ may locate at the position of NH_4^+ from $\text{NH}_4\text{V}_4\text{O}_{10}$ by co-sharing N elements and thus a smooth tunnel for the carrier's transfer will be established. Synchronously, the laminated NH_4^+ could be squeezed to the surface to increase the adsorptive sites toward target contaminants [27]. However, it is arduous task to insert $\text{g-C}_3\text{N}_4$ into interlamination of $\text{NH}_4\text{V}_4\text{O}_{10}$ to prepare the intercalated $\text{g-C}_3\text{N}_4/\text{NH}_4\text{V}_4\text{O}_{10}$ heterojunction. As we know, the interlaminar distance of $\text{NH}_4\text{V}_4\text{O}_{10}$ is slightly small, which is only about several to a dozen nanometer thickness [28]. Thus, in order to assemble an interlaminar $\text{NH}_4\text{V}_4\text{O}_{10}/\text{g-C}_3\text{N}_4/\text{NH}_4\text{V}_4\text{O}_{10}$ architecture, an ultrathin $\text{g-C}_3\text{N}_4$ is significantly required. Fortunately, in recent years, many methods of exfoliating bulk $\text{g-C}_3\text{N}_4$ to prepare very thin layered $\text{g-C}_3\text{N}_4$ have been developed [29–31]. The prepared materials have been applied in photodegradation of CIP and the activity, the applicable pollutant concentration, and the environmental tolerance have been carefully assessed. The mechanism of the enhanced photo-decontamination of CIP was investigated by estimating the migrated routes, the separation efficiency of photo-generated carriers, the steered adsorption toward target pollutants, and the reactive active sites of the prepared samples. This work shows that the in situ assembled $\text{g-C}_3\text{N}_4/\text{NH}_4\text{V}_4\text{O}_{10}$ can effectively decontaminate fluorquinolones by adsorption-photodegradation approach, and this method can be extended to the other removal of the fluoric contaminants in aqueous environment.

2. Experimental Section

2.1. Chemicals and Materials

All chemical reagents used in this investigation are analytical grade and the water is deionized from laboratory preparation. The characteristic and CAS number of the used regents are listed in Table S1.

2.2. Fabrication of $\text{NH}_4\text{V}_4\text{O}_{10}$

The 2D ultrathin $\text{NH}_4\text{V}_4\text{O}_{10}$ nanobelts were synthesized according to our previous publication [28] and the details are listed in supporting information (Text S1. Experimental section).

2.3. Fabrication of 2D ultrathin $\text{g-C}_3\text{N}_4$ nanosheets (CNNS)

The preparation of ultrathin 2D $\text{g-C}_3\text{N}_4$ nanosheets (CNNS) photocatalyst is achieved by the secondary calcination method. The specific method is as follows: First, place 5 g of urea in a crucible with a lid, and then tightly wrap the crucible with aluminum foil. The heating rate was set at $273.5 \text{ K}\cdot\text{min}^{-1}$ and the temperature were elevated up to 823 K. Then, the samples were calcined for three hours in a muffle furnace, naturally cooled down to room temperature, and then it was taken out to grind. Afterwards, the ground yellow powder was placed in an open crucible and calcined again. The temperature was increased to 773 K at a heating rate of $278 \text{ K}\cdot\text{min}^{-1}$ in a muffle furnace, and then it was calcined at 773 K for three hours. The obtained light-yellow powder was collected and named as CNNS.

2.4. Fabrication of CNNS/ $\text{NH}_4\text{V}_4\text{O}_{10}$

The simple process of CNNS/ $\text{NH}_4\text{V}_4\text{O}_{10}$ photocatalyst preparation is shown in Fig. 1. First, 0.5 g of 2D ultrathin CNNS nanosheets and 100 mL of deionized water were put into a 250 mL three-necked flask, sonicated for five minutes, and continued stirring for 1 h at 353 K. Then, 0.5 g of $\text{NH}_4\text{V}_4\text{O}_{10}$ was added to the suspension and the solution was continuously stirred at 353 K for 5 h. After slowly reducing to room temperature, the precipitate was collected by centrifugal filtration and washing, and then dried in a constant temperature oven at 333 K for 10 h. Finally, CNNS/ $\text{NH}_4\text{V}_4\text{O}_{10}$ was obtained by grinding. Different percentage ratio of CNNS/ $\text{NH}_4\text{V}_4\text{O}_{10}$ was prepared by varying the amount of CNNS (30 wt%, 50 wt% and 70 wt%) and named as 30-CNNS/ $\text{NH}_4\text{V}_4\text{O}_{10}$, 50-CNNS/ $\text{NH}_4\text{V}_4\text{O}_{10}$ and 70-CNNS/ $\text{NH}_4\text{V}_4\text{O}_{10}$, respectively.

2.5. Details of the activity assessment and characterization

Details of the activity assessment and characterization were presented in supporting information (Text S1. Experimental section).

3. Results and Discussion

3.1. Structure and morphologies of the prepared samples

The phase structures of CNNS, $\text{NH}_4\text{V}_4\text{O}_{10}$ and CNNS/ $\text{NH}_4\text{V}_4\text{O}_{10}$ nanocomposites were obtained through XRD analysis (Fig. 2a and Fig.S1). It can be clearly observed from Fig. 2a that there is a strong broad peak near 27.7° while a weaker peak near 13.2° for CNNS. The diffraction peak near 27.7° corresponds to the interlayer stacking of C_3N_4 nanosheets and can be indexed as a typical (0 0 2) peak. This relatively wide peak is explained as the layered structure of CNNS [32]. In addition, the wide and weak peak near 13.2° corresponds to the (1 0 0) peak of CNNS, due to the in-plane porous structure formed by the ultra-thin C_3N_4 nanosheets (JCPDS No. 87-1526) [33,34]. At the same time, the diffraction peaks of the pure $\text{NH}_4\text{V}_4\text{O}_{10}$ completely conform to the structure of monoclinic phase $\text{NH}_4\text{V}_4\text{O}_{10}$ (JCPDS No. 31-0075) [35]. For all 2D/2D structure of CNNS/ $\text{NH}_4\text{V}_4\text{O}_{10}$ nanocomposites, the signals all assign to the characteristic peaks of both CNNS and $\text{NH}_4\text{V}_4\text{O}_{10}$, inferring no impurity existence. The peaks at 13.2° presents very weak in the composite, which is considered as the covering by the well crystalline $\text{NH}_4\text{V}_4\text{O}_{10}$. In addition, although the peaks at 27.7° of CNNS and the two diffraction peaks at 27.7 and 28.1° of $\text{NH}_4\text{V}_4\text{O}_{10}$ are highly overlapped, it can be seen that this peak is gradually enhanced with the introduction of CNNS (Fig.S1). Moreover, the strong diffraction peak of 2-theta located at 9.16° is significantly reduced by introducing CNNS. Combining with these data, the formation

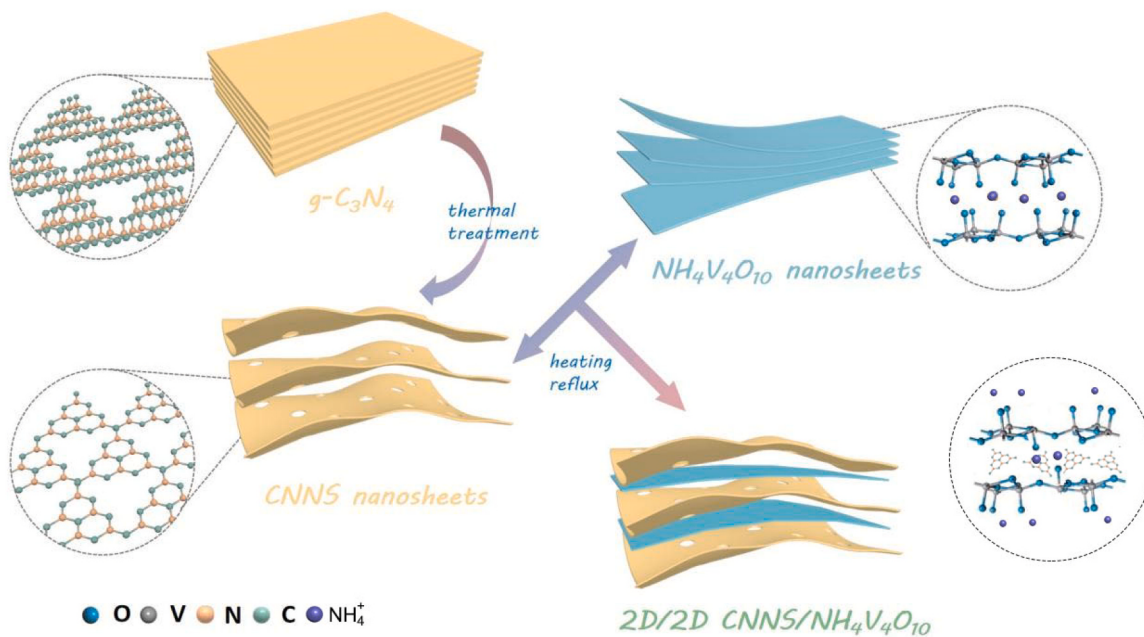


Fig. 1. The fabrication process of 2D/2D CNNS/ $\text{NH}_4\text{V}_4\text{O}_{10}$ nanocomposite.

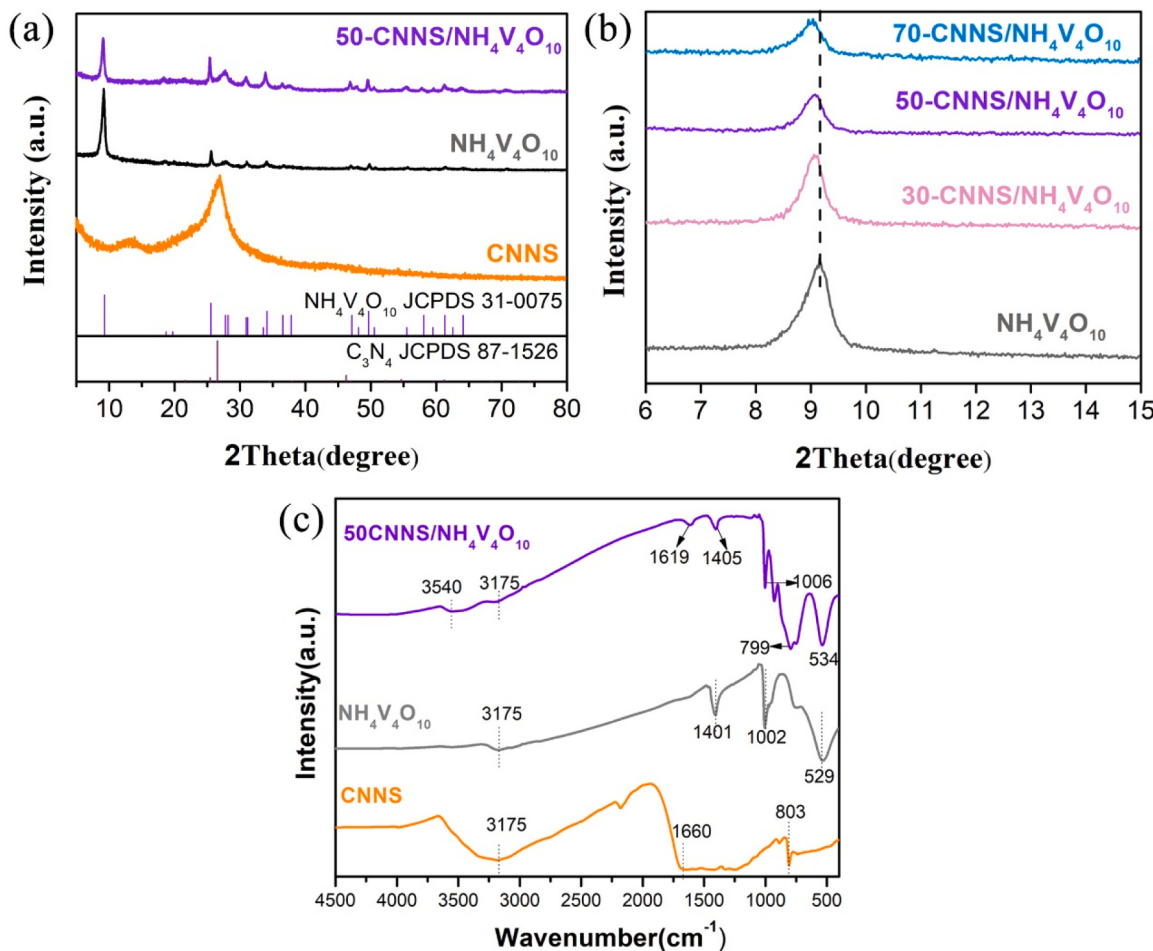


Fig. 2. XRD pattern (a, b) and FT-IR spectra (c) for the as-prepared CNNS, $\text{NH}_4\text{V}_4\text{O}_{10}$ and CNNS/ $\text{NH}_4\text{V}_4\text{O}_{10}$ samples.

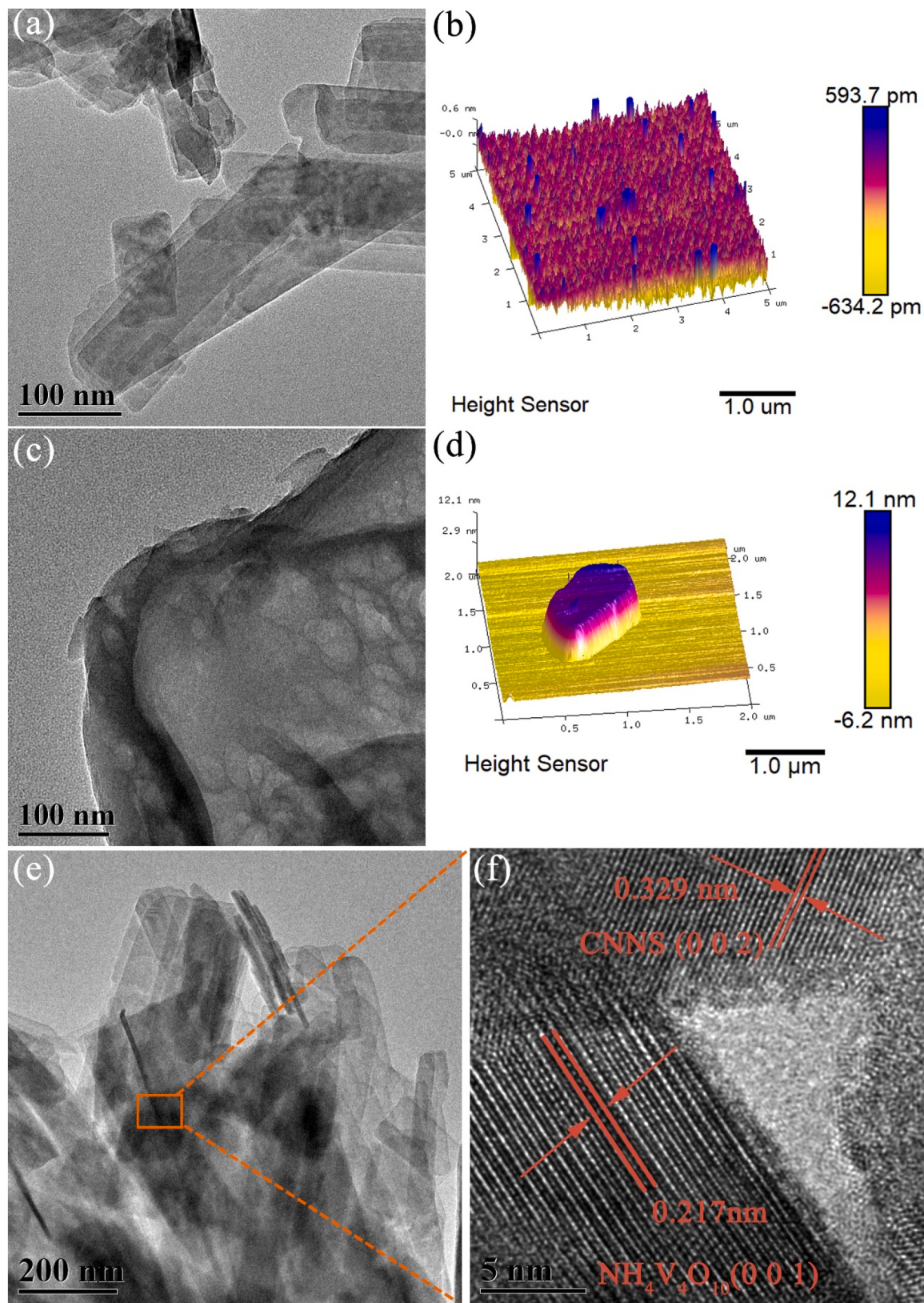


Fig. 3. TEM (a) and AFM (b) of $\text{NH}_4\text{V}_4\text{O}_{10}$, TEM (c) and AFM (d) of CNNS; TEM (e) and HRTEM (f) of 50-CNNS/ $\text{NH}_4\text{V}_4\text{O}_{10}$.

of $\text{C}_3\text{N}_4/\text{NH}_4\text{V}_4\text{O}_{10}$ composites is well confirmed. According to the 2-theta position on the (0 1 0) crystal plane of $\text{NH}_4\text{V}_4\text{O}_{10}$, the calculated interlaminar distance of $\text{NH}_4\text{V}_4\text{O}_{10}$, 30-CNNS/ $\text{NH}_4\text{V}_4\text{O}_{10}$, 50-CNNS/ $\text{NH}_4\text{V}_4\text{O}_{10}$, 70-CNNS/ $\text{NH}_4\text{V}_4\text{O}_{10}$ samples were 0.963 nm, 0.973 nm, 0.977 nm and 0.980 nm, respectively, indicating the increase of interlayer. Obviously, this increased interlaminar distance is originated from the intercalation of CNNS, expanding the two (0 1 0) planes of $\text{NH}_4\text{V}_4\text{O}_{10}$ [36–38]. The FT-IR spectra of CNNS, $\text{NH}_4\text{V}_4\text{O}_{10}$ and 50CNNS/ $\text{NH}_4\text{V}_4\text{O}_{10}$ composites are shown in Fig. 2c. For CNNS, 1660 cm^{-1} , 807 cm^{-1} are attributed to the C=N bond and the bending vibration of heptazine unit [39,40], the board peak at 3175 and 3258 cm^{-1} are corresponded to the stretching vibrations of O-H groups in surface and N-H of CNNS aromatic rings respectively [41]. As for $\text{NH}_4\text{V}_4\text{O}_{10}$, the 529 cm^{-1} and 1002 cm^{-1} peaks are compatible with the symmetric stretching vibration of V-O-V and V=O stretching vibration [42], the absorption band at 1401 cm^{-1} and 3175 are ascribed to the N-H in-plane bending vibration and N-H stretching vibration of the NH_4^+ group [43]. It is obvious that the CNNS/ $\text{NH}_4\text{V}_4\text{O}_{10}$ composite samples show both characteristic peaks of CNNS and $\text{NH}_4\text{V}_4\text{O}_{10}$. Notably, those peaks in the CNNS/ $\text{NH}_4\text{V}_4\text{O}_{10}$ composite display a slight red shift from those for pure $\text{NH}_4\text{V}_4\text{O}_{10}$ and a slight blue shift for pure CNNS, revealing the successful assembly of the separated components and the existence of a strong interaction between CNNS and $\text{NH}_4\text{V}_4\text{O}_{10}$.

SEM, TEM and AFM were carried out to characterize the morphology and microstructure of the photocatalysts in Fig. 3 and Fig. S2. In the TEM image (Fig. 3a) and SEM image (Fig. S2a), it can be clearly seen that the as-prepared $\text{NH}_4\text{V}_4\text{O}_{10}$ exhibit an 2D ultra-thin nanobelts structure, which is very smooth and uniformly stacked together. Furthermore, its ultra-thin characteristics was confirmed by AFM image in Fig. 3b, which presents a thickness of about 0.6 to 0.9 nm. Withal, CNNS also shows a

very typical ultra-thin layer structure with a thickness of approximately 10 nm (Figs. 3c, 3d and Fig. S2b). At the same time, it can be observed that CNNS nanosheets are sculptured as the affluent nanopore (about 15 nm in diameter) in the entire nanosheets area compared to bulk C_3N_4 , and the volume of the layered CNNS was relatively expanded. Furthermore, for the as-prepared 50-CNNS/ $\text{NH}_4\text{V}_4\text{O}_{10}$, the two types of 2D ultra-thin layer materials have been well composited, and it presents a good dispersion effect without very serious accumulation (Fig. 3e, Fig. S2c). In Fig. 3f, the 50-CNNS/ $\text{NH}_4\text{V}_4\text{O}_{10}$ photocatalyst was tested by HRTEM. The lattice fringes of the two components can be clearly seen, $d = 0.217 \text{ nm}$ and 0.329 nm correspond to the (0 0 1) plane of $\text{NH}_4\text{V}_4\text{O}_{10}$ and (0 0 2) plane of CNNS, respectively, which can confirm the coexistence of two materials.

The prepared CNNS, $\text{NH}_4\text{V}_4\text{O}_{10}$ and 50-CNNS/ $\text{NH}_4\text{V}_4\text{O}_{10}$ nanocomposites were examined by XPS (Fig. 4). As showed in Fig. 4a, the N, V, C and O elements are checked in 50-CNNS/ $\text{NH}_4\text{V}_4\text{O}_{10}$ whereas it is only found C and N elements for CNNS and N, V, O elements for $\text{NH}_4\text{V}_4\text{O}_{10}$. Furthermore, the bonding energy of C 1 s of CNNS is located at 288.1 eV and 284.7 eV (Fig. 4b), attributed to the coordination between nitrogen atoms and carbon atoms [44]. The N 1 s peaks of CNNS with binding energies at 398.6 eV and 400.4 eV (Fig. 4c) can be attributed to sp^2 hybridization with C-N = C and N – (C)₃ coordination [45,46]. Compared with CNNS, the binding energies of N 1 s in 50-CNNS/ $\text{NH}_4\text{V}_4\text{O}_{10}$ are negatively shifted after the formation of heterojunctions, inferring more electron density in CNNS of the composite. Instead, the binding energy at 401.04 eV in $\text{NH}_4\text{V}_4\text{O}_{10}$ ascribed to the presence of NH_4^+ [47], have obviously shifts to high energy in 50-CNNS/ $\text{NH}_4\text{V}_4\text{O}_{10}$ (Fig. 4c), indicating a clear change of the chemical environment of NH_4^+ . It infers that NH_4^+ ions exist on the nanobelt

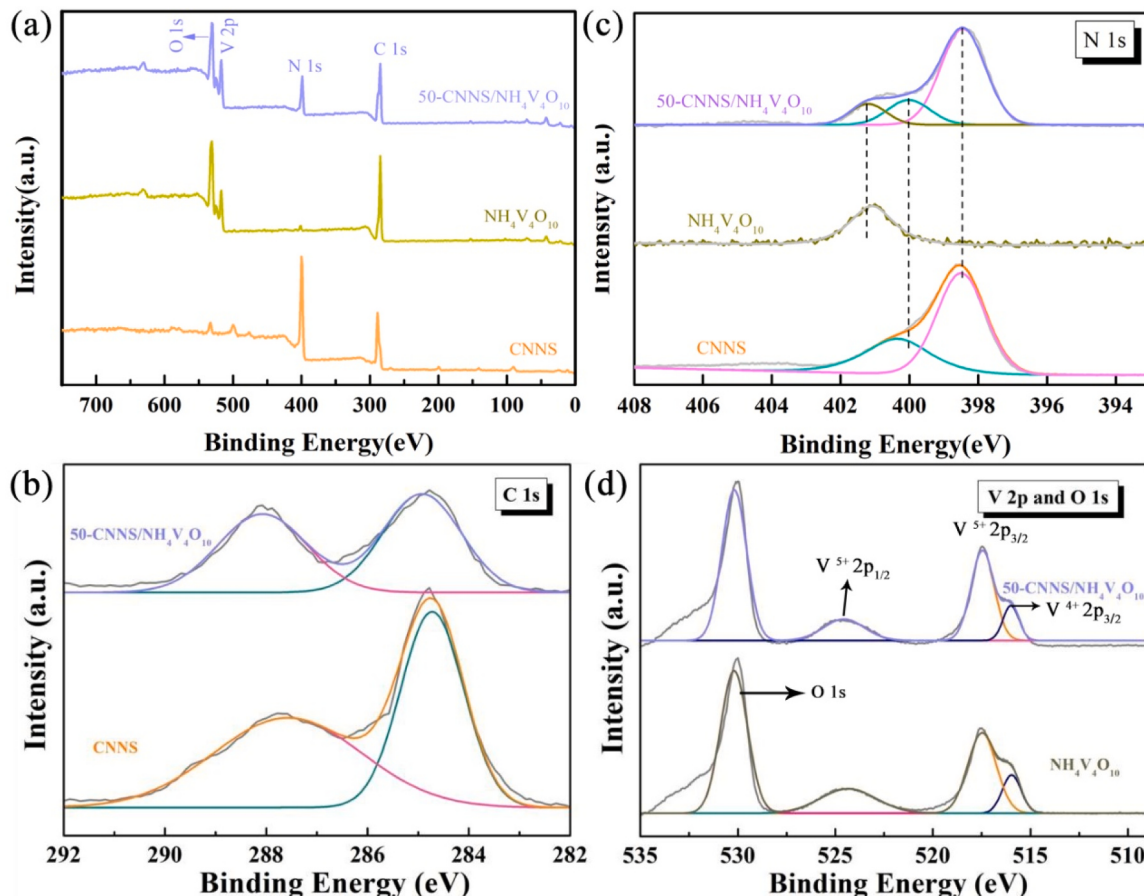


Fig. 4. XPS of the synthesized CNNS, $\text{NH}_4\text{V}_4\text{O}_{10}$ and CNNS/ $\text{NH}_4\text{V}_4\text{O}_{10}$: (a) Survey, (b) C 1 s, (c) N 1 s of CNNS and CNNS/ $\text{NH}_4\text{V}_4\text{O}_{10}$, (d) O 1 s and V 2p of $\text{NH}_4\text{V}_4\text{O}_{10}$ and CNNS/ $\text{NH}_4\text{V}_4\text{O}_{10}$.

surface of $\text{NH}_4\text{V}_4\text{O}_{10}$ via H-bonding. Meanwhile, the high-resolution XPS spectrum of V 2p in Fig. 4d shown the coexistence of V^{4+} and V^{5+} in $\text{NH}_4\text{V}_4\text{O}_{10}$ and 50-CNNS/ $\text{NH}_4\text{V}_4\text{O}_{10}$ [48], where the binding energies 524.5 eV, 517.6 eV and 516.1 eV, are indexed to V^{5+} 2p_{1/2}, V^{5+} 2p_{3/2} and V^{4+} 2p_{3/2}, respectively. In the XPS of O 1 s (Fig. 4d), the peaks at 530.0 eV in both $\text{NH}_4\text{V}_4\text{O}_{10}$ and 50-CNNS/ $\text{NH}_4\text{V}_4\text{O}_{10}$ is assigned to O^{2-} in the V-O bond [49]. Clearly, these XPS analysis can prove the perfect composite of ultra-thin CNNS nanosheets and $\text{NH}_4\text{V}_4\text{O}_{10}$ nanobelts, agreement with the conclusions of XRD and HRTEM.

3.2. Photocatalytic activity and stability

Under the condition of CIP concentration ($20 \text{ mg}\cdot\text{L}^{-1}$) and photocatalyst content ($0.5 \text{ g}\cdot\text{L}^{-1}$), the CIP degradation activity of the as-prepared CNNS, $\text{NH}_4\text{V}_4\text{O}_{10}$ and CNNS/ $\text{NH}_4\text{V}_4\text{O}_{10}$ were evaluated (Fig. 5a). Firstly, the degradation of CIP is almost not occurred without the light irradiation in the case of no any photocatalysts presentence. Next, the blank experiments of photolysis and adsorption presented in Fig.S3 reveal that the concentration of CIP is not altered in the absence of photocatalyst, which verifies the photochemical stability of CIP under simulated sunlight irradiation. The result under dark condition shows that 75% CIP is absorbed by 50-CNNS/ $\text{NH}_4\text{V}_4\text{O}_{10}$ and the adsorption equilibrium is reached as the adsorption time increases to 40 mins. Furthermore, pure CNNS and $\text{NH}_4\text{V}_4\text{O}_{10}$ show slight low activity for the photocatalytic degradation of CIP that is 72% within 120 min for $\text{NH}_4\text{V}_4\text{O}_{10}$ and is 79% for CNNS. However, for the composite CNNS/ $\text{NH}_4\text{V}_4\text{O}_{10}$, the photocatalytic efficiency is well improved and the optimized 50-CNNS/ $\text{NH}_4\text{V}_4\text{O}_{10}$ presents the best degradation performance with a 95% degradation rate within 100 min for CIP. Furthermore, the kinetics constant was obtained by the best fitted first-order kinetics

curves of CIP (Fig. 5b) [50]. As shown in this figure, CNNS has the optimal photoreaction rate, which is mainly due to its limited adsorption capacity (only able to adsorb 19% of the CIP solution), while degrading CIP from 19% to 79% after the light was turned on, whereas, after complexing with ammonium vanadate, 50-CNNS/ $\text{NH}_4\text{V}_4\text{O}_{10}$ has excellent adsorption capacity, and is able to continuously degrade CIP from 80% to more than 95% after the lighting with a high degradation and mineralization capacity. Furthermore, in considering the widely range of CIP residues from ppb in the ground water to the ppm or even higher in the industrial discharge wastewater, thus the removal efficiency of various CIP concentrations on the synthesized 50-CNNS/ $\text{NH}_4\text{V}_4\text{O}_{10}$ sample was investigated here (Fig. 5c). The test was implemented with different CIP concentrations of $5 \text{ mg}\cdot\text{L}^{-1}$, $10 \text{ mg}\cdot\text{L}^{-1}$, $20 \text{ mg}\cdot\text{L}^{-1}$, $30 \text{ mg}\cdot\text{L}^{-1}$, $40 \text{ mg}\cdot\text{L}^{-1}$, and $50 \text{ mg}\cdot\text{L}^{-1}$ under simulated sunlight with $0.5 \text{ g}\cdot\text{L}^{-1}$ 50-CNNS/ $\text{NH}_4\text{V}_4\text{O}_{10}$. It is clearly the catalyst is effective in CIP concentrations range from $5 \text{ mg}\cdot\text{L}^{-1}$ to $20 \text{ mg}\cdot\text{L}^{-1}$, where the degradation rate is 96.8% and 91.4%, respectively. Whereas, it will be gradually descended to 85.6%, 80.5% and 68.5% for CIP concentration of $30 \text{ mg}\cdot\text{L}^{-1}$, $40 \text{ mg}\cdot\text{L}^{-1}$, and $50 \text{ mg}\cdot\text{L}^{-1}$, respectively.

Afterwards, the dosage of the as-prepared samples was tested by 50-CNNS/ $\text{NH}_4\text{V}_4\text{O}_{10}$ and the initial concentration of CIP is set at $20 \text{ mg}\cdot\text{L}^{-1}$. The results show the removal rate of CIP is increased from 78.1% to 84.1% and 91.4% within 120 min under simulated sunlight when the dosage is increased from $0.3 \text{ g}\cdot\text{L}^{-1}$ to $0.5 \text{ g}\cdot\text{L}^{-1}$. However, if the dosage goes beyond $0.5 \text{ g}\cdot\text{L}^{-1}$, the CIP removal rate is reduced and it is 88.1% for $0.6 \text{ g}\cdot\text{L}^{-1}$ dosage. This phenomenon could be assigned to the turbid reactive solution caused by the higher photocatalyst dosage, thereby inhibiting the absorption of light. Thus, the optimal photocatalyst dosage was determined to be $0.5 \text{ g}\cdot\text{L}^{-1}$, which provided a very important inspiration for achieving more efficient and economical

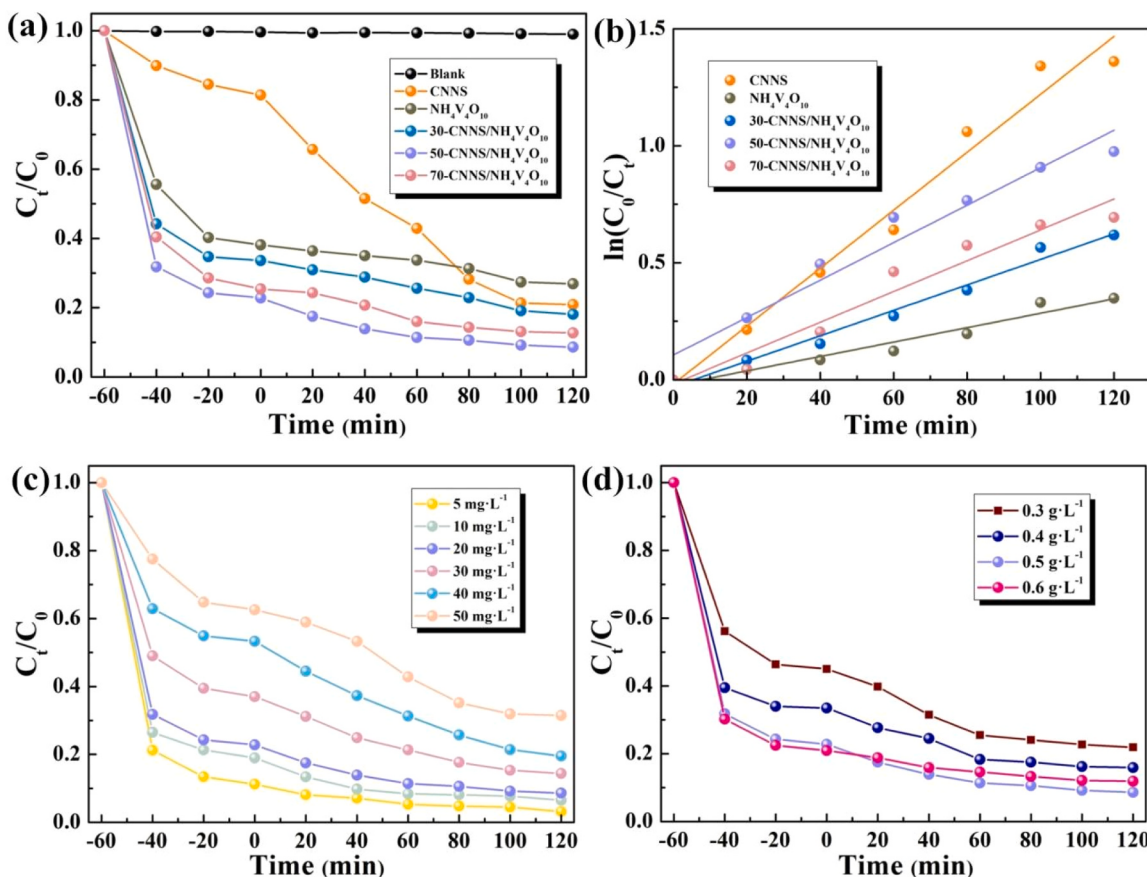


Fig. 5. (a) Photo-degradation rates and (b) kinetics curves of obtained catalysts (photocatalyst dosage = $0.5 \text{ g}\cdot\text{L}^{-1}$, CIP = $20 \text{ mg}\cdot\text{L}^{-1}$), (c) photo-degradation rates of 50-CNNS/ $\text{NH}_4\text{V}_4\text{O}_{10}$ with different CIP initial concentration (photocatalyst dosage = $0.5 \text{ g}\cdot\text{L}^{-1}$), and (d) different dosage (CIP = $20 \text{ mg}\cdot\text{L}^{-1}$).

photodegradation of CIP.

In order to understand the stability of 50-CNNS/NH₄V₄O₁₀, a recycle of photodegradation of CIP was implemented (CIP concentration was 20 mg·L⁻¹). Fig. S4a was the result after five cycles of experiments. The photocatalytic activities of CNNS and NH₄V₄O₁₀ decreased significantly after five cycles whereas the 50-CNNS/NH₄V₄O₁₀ photocatalyst still maintains a high photodegradation efficiency of CIP, inferring its good reusability. The structure stability was further confirmed by the changeless peak positions in XRD for the initial samples and the one after the five recycle tests (Fig. S4b). To worried about the leaching of V, which is deleterious to environment, vanadium content in the solution before and after reaction has been detected with ICP. It is found the vanadium concentration is 0.000633 mg/L and 0.0668 mg/L in the solution before and after recycled reaction, respectively, indicating that a small amount vanadium would be dissolved in the solution in the degradation process. As it knows, the maximum vanadium content in drinking water and industrial water is 0.1 mg/L and 1 mg/L, respectively. Therefore, the trace V dissolution meets the drinking water standard and does not cause pollution of the water environment. Summarily, it can be expected 50-CNNS/NH₄V₄O₁₀ photocatalyst presents not only excellent photocatalytic activity but also good photocatalytic stability, which lays a solid foundation for the practical applications.

The photocatalytic details of CIP degradation were explored, and the total organic carbon (TOC) test was performed on CNNS, NH₄V₄O₁₀ and 50-CNNS/NH₄V₄O₁₀ photocatalysts (Table S2). As the results show, the total organic carbon of all samples is decreased while the total inorganic carbon is increased during the whole test process. Moreover, 50-CNNS/NH₄V₄O₁₀ shows the highest mineralization ability for CIP among all samples which can reach 58% mineralization efficiency. Withal, the mineralization efficiency is found not as high as the photodegradation efficiency, which is attributed to CIP cannot be completely mineralized

to generate CO₂ and H₂O. Inversely, many small organic molecules were produced during the reaction process [51]. Nevertheless, for 50-CNNS/NH₄V₄O₁₀ the most excellent photodegradation and mineralization activity among the separated pure samples and the composites prove the significantly improved performance by the formation of the 2D/2D ultra-thin nanocomposite structure. The probable intermediates formed in the CIP photodegradation process were identified by the mass spectrometry (MS). Among them, the intermediates rest at M/Z at 304, 293, 275, 220, 175, 148, 125, 114, 102, 84 are showed in Fig. S5. Based on previous research, three possible degradation paths have been proposed and shown in Fig. S5c [52–54], where CIP molecules undergo decarboxylation, defluorination, decarbonylation, hydroxylation reactions and ring-opening reactions of quinolone ring, piperazinyl ring and benzene ring under the attack of active species. Finally, these small organic species are further mineralized into CO₂ and H₂O.

3.3. The mechanism investigation

The light absorptive performance is very importance in the photocatalytic reaction, thus it is tested by UV-vis diffuse reflectance spectroscopy (DRS) for the as-prepared CNNS, NH₄V₄O₁₀ and CNNS/NH₄V₄O₁₀ (Fig. 6a). Clearly, both the composites and the separated components respond broad-spectrum absorption in the ultraviolet, visible, and even near-infrared regions, which relates to their excellent photocatalytic ability. Furthermore, the optical band gap of the as-prepared photocatalyst are calculated by the Tauc's Equation: $(\alpha h\nu)^2 = A(h\nu - E_g^n)$ [55], as shown in Fig. 6a, being 2.33 eV, 2.29 eV, 2.22 eV, 2.19 eV and 2.21 eV for CNNS, NH₄V₄O₁₀, 30-CNNS/NH₄V₄O₁₀, 50-CNNS/NH₄V₄O₁₀ and 70-CNNS/NH₄V₄O₁₀, respectively. In order to determine the transfer ability of photo-generated carriers of the prepared samples in the photodegradation of CIP, the fluorescence (PL)

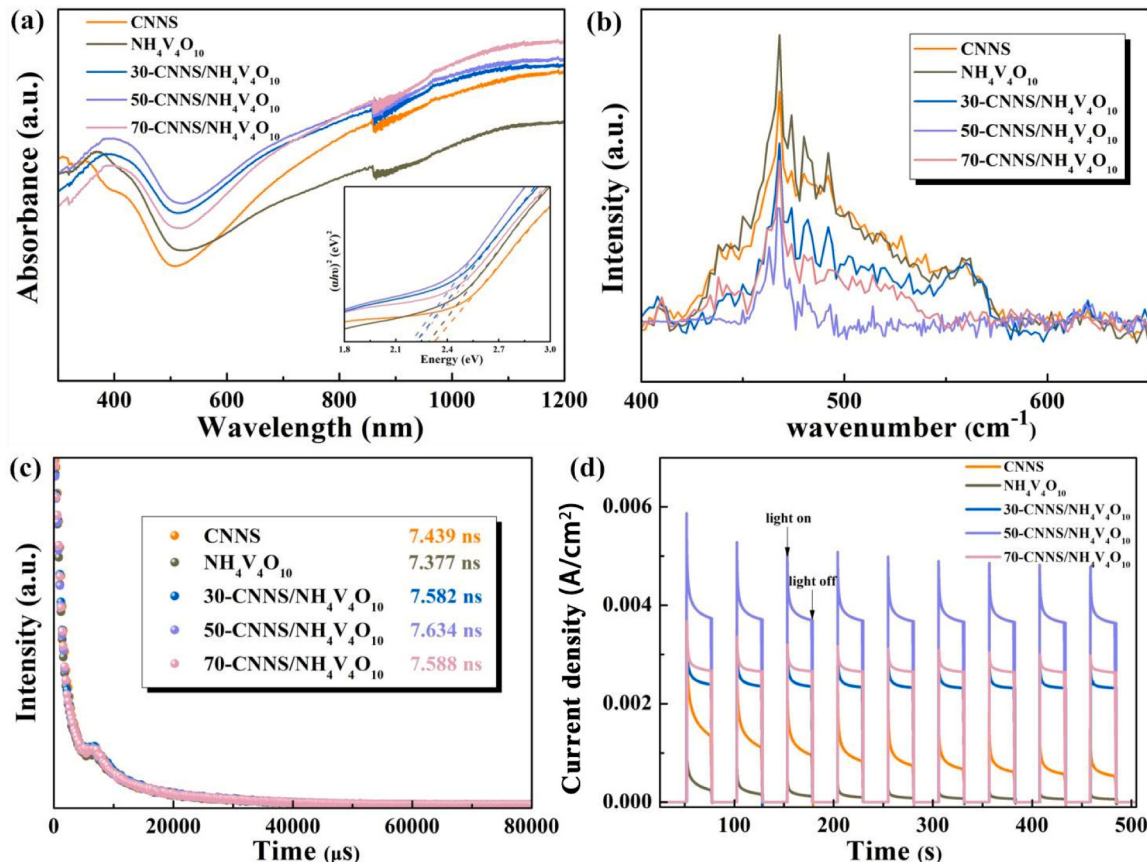


Fig. 6. (a) UV-vis absorption and the insert is the band gap, (b) photoluminescence, (c) the time-resolved fluorescence spectra excited at 327 nm, and (d) transient photocurrent response for CNNS, NH₄V₄O₁₀ and CNNS/NH₄V₄O₁₀.

spectra of CNNS, $\text{NH}_4\text{V}_4\text{O}_{10}$ and CNNS/ $\text{NH}_4\text{V}_4\text{O}_{10}$ were characterized (Fig. 6b). As it is known, the efficiency of photogenerated charge transfer or recombination can be reflected by the excitation strength of the PL spectrum [56]. It can be observed that the as-prepared CNNS, $\text{NH}_4\text{V}_4\text{O}_{10}$ and CNNS/ $\text{NH}_4\text{V}_4\text{O}_{10}$ all show a PL emission peak at an excitation wavelength of 315 nm. The photoluminescence intensity of 50-CNNS/ $\text{NH}_4\text{V}_4\text{O}_{10}$ photocatalyst is much weaker compared with other samples, which is a good proof that the recombination probability of its photogenerated carriers will be reduced. In addition, the PL spectrum intensity of all CNNS/ $\text{NH}_4\text{V}_4\text{O}_{10}$ nanocomposite is lower than that of pure CNNS and $\text{NH}_4\text{V}_4\text{O}_{10}$. This phenomenon also shows that after the formation of 2D/2D nanocomposite structure, the separation and transfer efficiency of photo-generated charge is significantly promoted and thus the recombination of photo-generated e^- - h^+ pair is well suppressed.

The improved photogenerated charge transfer and separation efficiency of the CNNS/ $\text{NH}_4\text{V}_4\text{O}_{10}$ photocatalyst can be further verified and analyzed based on transient fluorescence (TRPL) spectroscopy. Fitting the fluorescence decay curve based on the kinetic function principle can be obtained by Eqs. (1) and (2) [57]:

$$I(t) = I_0 + A_1 \exp\left(-\frac{t}{\tau_1}\right) + A_2 \exp\left(-\frac{t}{\tau_2}\right) \quad (1)$$

$$\tau = \frac{A_1 \tau_1^2 + A_2 \tau_2^2}{A_1 \tau_1 + A_2 \tau_2} \quad (2)$$

Among them, A_1 and A_2 represent the amplitude, and τ_1 and τ_2 are respectively defined as the corresponding emission lifetimes. The calculated average lifetime τ of the photogenerated carriers is shown in Fig. 6c. The 50-CNNS/ $\text{NH}_4\text{V}_4\text{O}_{10}$ photocatalyst have a higher average life span. Therefore, with the enhancement of the photogenerated charge separation process, the life of photogenerated carriers has been strongly prolonged. It is further proved that the photo-generated electrons and holes are better separated in CNNS/ $\text{NH}_4\text{V}_4\text{O}_{10}$, which will reduce the photo-generated charge recombination rate and further improved the photocatalytic activity.

The transient photocurrent response of the as-prepared CNNS, $\text{NH}_4\text{V}_4\text{O}_{10}$ and CNNS/ $\text{NH}_4\text{V}_4\text{O}_{10}$ were tested to characterize the recombination and transfer behavior of photo-generated carriers. It can be seen from Fig. 6d that the photocurrent density under visible light irradiation is significantly and effectively improved than in a dark environment. It can be seen the photocurrent quickly increases at the instant of light-on, and then rapidly decays, which has been assigned the poor electrical conductivity of the materials and the rapid combination of photo-carriers [58]. Nevertheless, among all the samples, 50-CNNS/ $\text{NH}_4\text{V}_4\text{O}_{10}$ photocatalyst shows the most significant effect in several light on-off cycles and presents a highest stable photocurrent value. Therefore, it gives a

conclusion the composite 50-CNNS/ $\text{NH}_4\text{V}_4\text{O}_{10}$ can realize the rapid transfer of the photo-generated electrons on the interface.

The electrochemical impedance (EIS) test was also used to study the charge transport properties and interface resistance of CNNS, $\text{NH}_4\text{V}_4\text{O}_{10}$ and CNNS/ $\text{NH}_4\text{V}_4\text{O}_{10}$ samples (Fig. 7). From the experimental results, the arc radius of the fitted EIS Nyquist diagram under light is smaller than that under the dark environment, which may be due to the formation of numerous photo-generated e^- - h^+ pairs in the photocatalyst under light irradiation [59]. Additionally, the arc radius of 50-CNNS/ $\text{NH}_4\text{V}_4\text{O}_{10}$ is the smallest among all the as-prepared samples, no matter in dark or light conditions. This result indicates that the 2D/2D photocatalyst could promote the transfer of photo-generated electrons, which consistent with the photocurrent response results.

Meanwhile, the reactive radical quenching and electron spin resonance (ESR) were implemented to prove the major species in CIP photodegradation with CNNS/ $\text{NH}_4\text{V}_4\text{O}_{10}$. In this test (Fig. S6), t-BuOH (1 mmol) and BQ (1 mmol) were used to capture $\cdot\text{OH}$ and $\cdot\text{O}_2^-$ radicals, while EDTA (1 mmol) and AgNO_3 (1 mmol) were used to capture photogenerated h^+ and e^- [60]. After adding BQ and t-BuOH, the photo-degradation rate of CIP is serious decreased, which shows a very key role of $\cdot\text{O}_2^-$ and $\cdot\text{OH}$ radicals in the photo-degradation of CIP with CNNS/ $\text{NH}_4\text{V}_4\text{O}_{10}$. Meanwhile, by quenching e^- and h^+ species with AgNO_3 and EDTA, the effect of photo-degradation of CIP is slightly reduced. It means the photo-generated e^- and h^+ will also affect the photocatalytic performance because the photo-generated e^- may generate $\cdot\text{O}_2^-$ with O_2 , and the h^+ will generate $\cdot\text{OH}$ with $\text{H}_2\text{O}/\text{OH}^-$.

To further reveal the carriers' performance, the electron paramagnetic resonance (EPR) and Kelvin probe atomic force microscopy (KPFM) were carried out for $\text{NH}_4\text{V}_4\text{O}_{10}$, CNNS, and 50-CNNS/ $\text{NH}_4\text{V}_4\text{O}_{10}$. As shown in Fig. 8, for the single $\text{NH}_4\text{V}_4\text{O}_{10}$, the typical peaks of DMPO- $\bullet\text{O}_2^-$ are not detected in methanol (Fig. 8a), whereas the peaks of DMPO- $\bullet\text{OH}$ have been observed in deionized water. It suggests that $\text{NH}_4\text{V}_4\text{O}_{10}$ possesses a lower reduction potential and a higher oxidation potential under visible light excitation. Furthermore, for CNNS, the typical peaks of DMPO- $\bullet\text{O}_2^-$ have been found but the peaks of DMPO- $\bullet\text{OH}$ are not detected (Fig. 8b), suggesting that CNNS has strong reducing performance instead of oxidizing ability. For the composite 50-CNNS/ $\text{NH}_4\text{V}_4\text{O}_{10}$, both the EPR signals of DMPO- $\bullet\text{O}_2^-$ and DMPO- $\bullet\text{OH}$ are exhibited in Fig. 8a and b, revealing its strong redox abilities. By combining the active species data, obviously, the photo-excited carriers transfer via a S-scheme path (Fig. S7) [61]. To clarify this point, KPFM is tested and the corresponding images of CNNS and $\text{NH}_4\text{V}_4\text{O}_{10}$ are shown in Fig. 9a and b. Further, the fitted surface potentials are shown in Fig. 9c and d. It can be seen the surface potential for $\text{NH}_4\text{V}_4\text{O}_{10}$ (4.49 V) is much higher than CNNS (3.77 V), which indicates that the electrons will transport from $\text{NH}_4\text{V}_4\text{O}_{10}$ to CNNS [62]. Hence, the photoelectrons generated in the heterojunction are proposed to transfer based on the

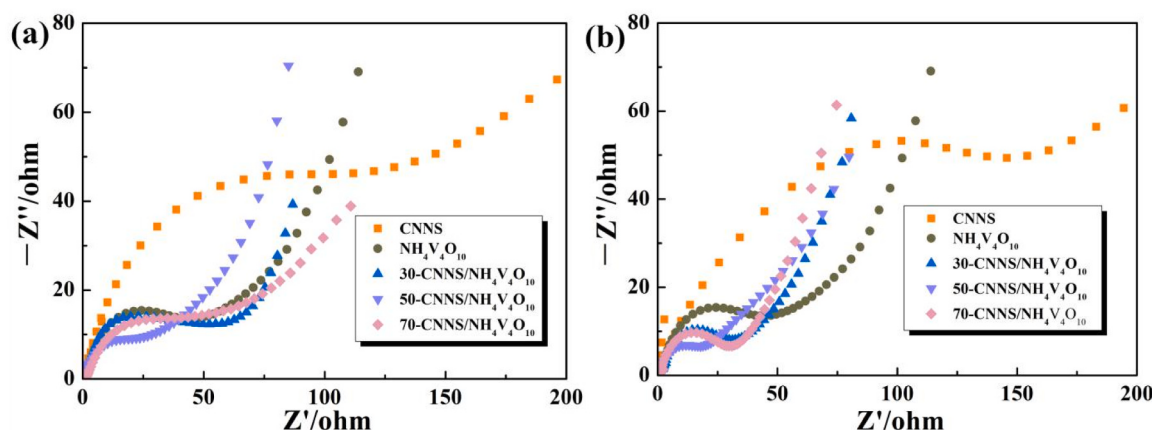


Fig. 7. EIS spectra of CNNS, $\text{NH}_4\text{V}_4\text{O}_{10}$ and CNNS/ $\text{NH}_4\text{V}_4\text{O}_{10}$ in dark (a) and with light irradiation (b).

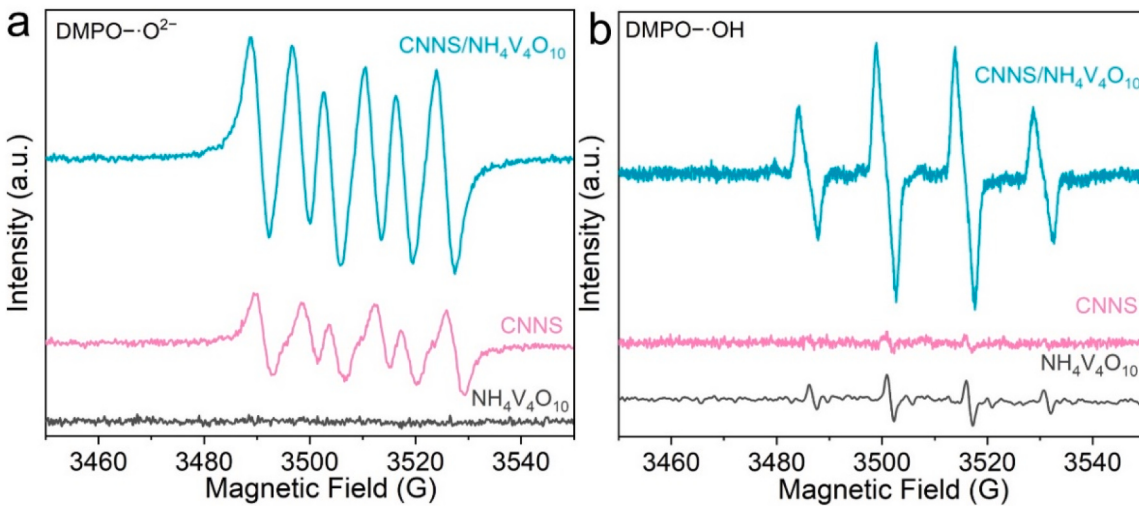


Fig. 8. EPR of NH₄V₄O₁₀, CNNS and 50-CNNS/NH₄V₄O₁₀ for (a) DMPO-·O₂⁻ and (b) DMPO-·OH.

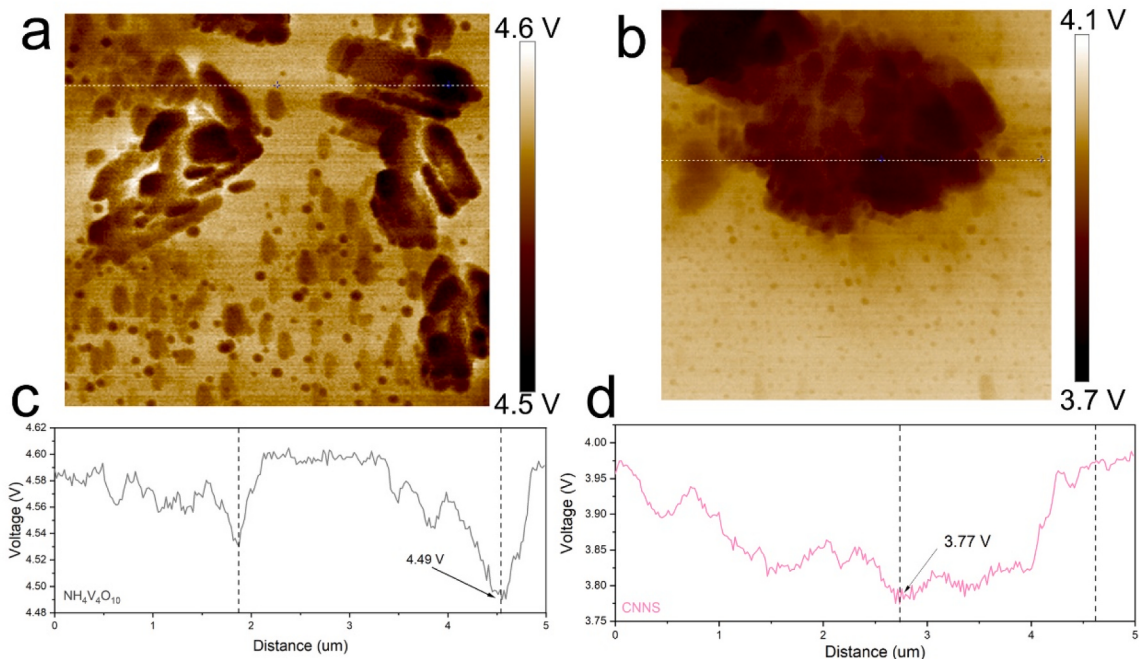


Fig. 9. KPFM images of (a) NH₄V₄O₁₀ and (b) CNNS; the measured surface potential profiles of (c) NH₄V₄O₁₀ and (d) CNNS.

S-scheme mechanism under illumination.

Further, the energy levels are carefully aligned in order to trace the carriers' transfer route (Fig. S7). Firstly, the valence band level was obtained by XPS valence band spectra (Fig. S8), and the band edge energy of CNNS and NH₄V₄O₁₀ are + 2.68 V and + 1.98 V (vs NHE) from the UV-vis data (Fig. 6a). Then, the conduction bands level of CNNS and NH₄V₄O₁₀ are calculated to be 0.39 and - 0.35 V (vs NHE) by formula $E_{CB} = E_{VB} - E_g$ [63]. As the discussion above, the NH₄V₄O₁₀/CNNS composite can produce both ·O₂ and ·OH and thus it means the composite possesses both high oxidized and reduced ability. Thus, a S-type transfer pathway is proposed, in which the photo-generated electrons from NH₄V₄O₁₀ with a higher band potential flow to a lower surface potential of CNNS to combine with the holes there (Fig. S7). As a result, the energy levels of NH₄V₄O₁₀ shifts down whereas those of C₃N₄ moves up, leading to the bending of the band edge. Therefore, the electrons in the CB of CNNS and the holes in the VB of NH₄V₄O₁₀, have been well spatially separated, presenting the electrons' higher reduction in the CB of CNNS

and the good oxidative performance of holes in VB of NH₄V₄O₁₀. In this case, the band edge potential in reduced part of NH₄V₄O₁₀/CNNS is more negative than that of O₂/O₂⁻ (-0.046 eV) [64] and the electrons there can react with O₂ to produce ·O₂⁻. Meanwhile, the h⁺ in the oxidative part of the composite can also combine with H₂O/OH⁻ to generate ·OH radicals. Obviously, the proposed S-type heterojunction mechanism elucidates the shift and reactive routes of carriers, consistent with the results of the radical quenching test and EPR experiment.

By enriching organic molecules to improve the performance of photodegradation, the pre-adsorption capacity is very important for the removal of CIP. Thus, the adsorption capacity (the calculation formula seen [supporting information](#)) of the as-prepared CNNS, NH₄V₄O₁₀ and 50-CNNS/NH₄V₄O₁₀ photocatalysts were tested. As shown in Fig. 10a, the adsorption equilibrium is completed after standing in the dark for 40 min for 20 mg·L⁻¹ CIP, and as time passed, no further adsorption was observed. Obviously, 50-CNNS/NH₄V₄O₁₀ gives a highest adsorption capacity (30.88 mg·g⁻¹) among these samples. BET characterization

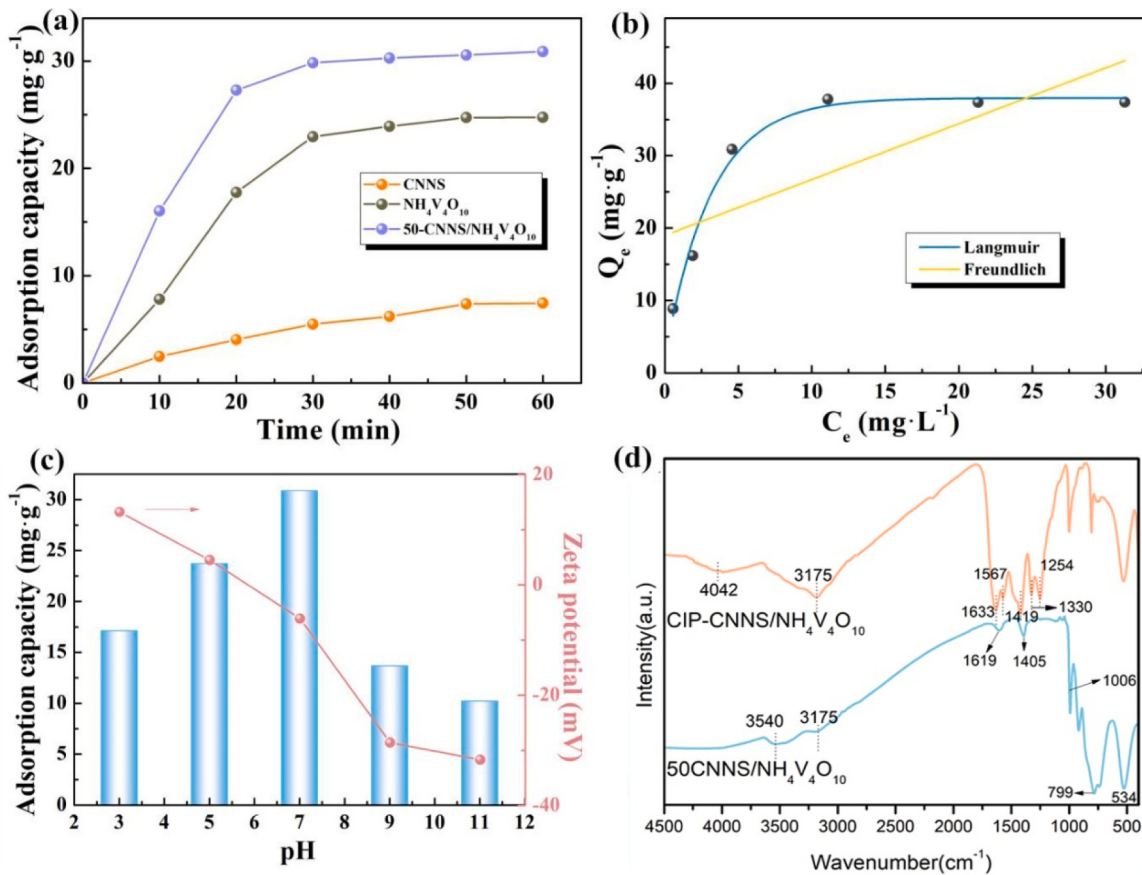


Fig. 10. (a) The adsorption capacity of CNNS, NH₄V₄O₁₀ and 50-CNNS/NH₄V₄O₁₀; (b) Adsorption isotherm of CIP by 50-CNNS/NH₄V₄O₁₀ sample; (c) Zeta potential of 50-CNNS/NH₄V₄O₁₀ and impression of pH on adsorption of CIP; (d) FTIR spectra of 50-CNNS/NH₄V₄O₁₀ composite before and after adsorption CIP.

results (Table S3) confirm that the 2D/2D structure of CNNS/NH₄V₄O₁₀ nanocomposite had a larger specific surface area. However, it is also found adsorption of CIP by CNNS is far below that by NH₄V₄O₁₀ although CNNS has a bigger BET. Thus, it is speculated that the steered adsorption via NH₄⁺ ions is far beyond than the physical adsorption through larger specific surface area [65]. In addition, by measuring the adsorption isotherm of CIP, it can be observed that as the equilibrium concentration of CIP increases from 0.56 to 11.1 mg·L⁻¹, the adsorption capacity (Q_e) increases almost linearly (Fig. 10b) and the saturated adsorption Q_e remains at about 37.4 mg·g⁻¹ in 50-CNNS/NH₄V₄O₁₀. Similarly, the adsorption capacities of 30-CNNS/NH₄V₄O₁₀ and 70-CNNS/NH₄V₄O₁₀, are 27.6 and 32.5 mg/g, respectively (Fig. S9). At the same time, the adsorption isotherm fit the Langmuir [66] equation well, indicating that the single-layer adsorption mode accurately represents the current adsorption behavior. Withal, the effect of different initial pH values (3, 5, 7, 9 and 11) on CIP adsorption (Fig. 10c) and photocatalytic degradation (Fig. S10) over 50-CNNS/NH₄V₄O₁₀ were also tested. In an acidic environment, CIP presents cationic form. Meanwhile, the zeta potential of the surface of 50-CNNS/NH₄V₄O₁₀ presents positive charge at pH< 5.8 (Fig. 10c). Thus, the strong electrostatic repulsion between CIP and the catalyst hampers the absorption of CIP. In a neutral solution, the adsorption capacity and degradation activity of 50-CNNS/NH₄V₄O₁₀ is higher while it drops slightly at a larger pH value (pH=11). It is reasonable that the acid NH₄⁺ ions may be quickly decreased in the basic environment. As we know, in this intercalation architecture, g-C₃N₄ may locate at the position of NH₄⁺ from NH₄V₄O₁₀ and thus the laminated NH₄⁺ could be squeezed to the surface to increase the adsorptive sites toward target contaminants [27]. To get insight into the contents of surface NH₄⁺, Nessler's Reagent Spectrophotometry was performed (Table S4), where the intercalation of the macromolecular structure of CNNS into the NH₄V₄O₁₀ results in the

absence and displacement of NH₄⁺. Thus, the NH₄⁺ content of CN NS/NH₄V₄O₁₀ samples (7879.49 mg/kg) is significantly lower compared to NH₄V₄O₁₀ (9949.66 mg/kg). Subsequently, the destination of the deficient NH₄⁺ was further explored by Zeta potentials measurements and it is found that the surface of NH₄V₄O₁₀ is markedly negatively charged (-36.67 mV), and the potential (-7.95 mV) became more positive after intercalation with CNNS. Thus, it is speculated that the displaced NH₄⁺ are reversed from the interior to the surface and the surface-enriched NH₄⁺ makes the composite catalyst surface take more positive charges, which is exactly combined with F⁻ from CIP and thus plays an essential role in the surface adsorption. To further determine the speculation, the FTIR spectra of the CNNS/NH₄V₄O₁₀ samples after adsorption of CIP are presented in Fig. 10d, the main characteristic peaks of CNNS/NH₄V₄O₁₀ are clearly displayed, more than that, there are some peaks presented in CIP-CNNS/NH₄V₄O₁₀, rather than CNNS/NH₄V₄O₁₀. Among those peaks, the absorption peak at 1254 cm⁻¹ were representative of the vibration of coupled carboxylic acid C-O stretch. The asymmetric vibration and symmetrical vibration peaks of -COO⁻ are reflected at 1567 and 1330 cm⁻¹, respectively [67]. Additionally, it is worth noting that the peak at 4042 cm⁻¹ was ascribed to the symmetrical stretching vibration of H-F band [68]. Thus, it is clear that the NH₄⁺ on the surface of the composite catalyst after intercalation is bonded to the F in the CIP molecule to obtain NH₄F, which can directly adsorb more CIP molecules and thus accelerate the reaction process.

In summary, the mechanism of CIP photo-degradation by CNNS/NH₄V₄O₁₀ photocatalyst under simulated sunlight are illustrated in Fig. 11. The enhanced photocatalytic activity is mainly attributed to the construction of the 2D/2D S-heterojunction, which can significantly improve the transfer efficiency of photo-generated electrons, giving an excellent electron transfer channel. And the combination of 2D ultrathin

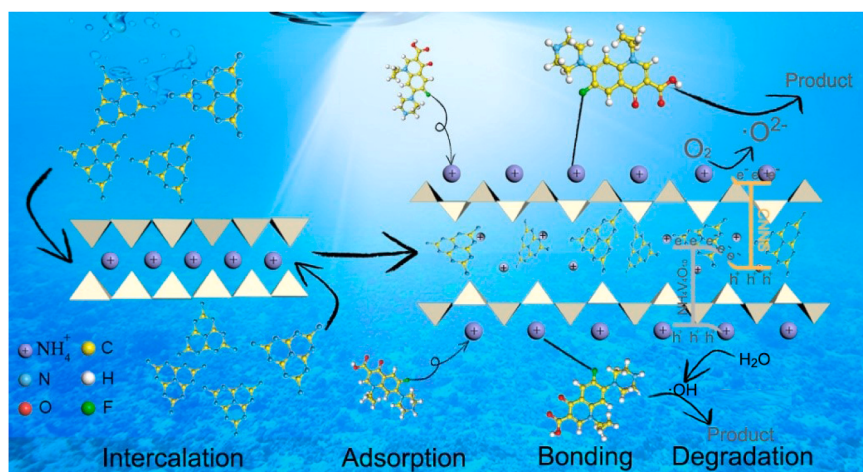


Fig. 11. The possible mechanism of the removal of CIP by CNNS/ $\text{NH}_4\text{V}_4\text{O}_{10}$ nanocomposite under simulate solar light illumination.

CNNS nanosheets and 2D ultrathin $\text{NH}_4\text{V}_4\text{O}_{10}$ nanobelts can provide more sufficient reactive sites. In this structure, CNNS is intercalated into the interior of $\text{NH}_4\text{V}_4\text{O}_{10}$ to break the interlayer bonding of NH_4^+ , which is subsequently squeezed onto the surface to establish more surface active sites thereby increasing the adsorption of the target pollutants and accelerating the rapid degradation of CIP pollutant molecules through bonding with F^- .

4. Conclusion

With *in situ* assembling technology, a series of interlaminar 2D/2D nanosheet heterojunction CNNS/ $\text{NH}_4\text{V}_4\text{O}_{10}$ has been prepared and their photocatalytic activity were assessed by photo-degradation of CIP. The optimized 50-CNNS/ $\text{NH}_4\text{V}_4\text{O}_{10}$ presents the best removal rate of 92% for $10 \text{ mol}\cdot\text{L}^{-1}$ CIP under simulated solar light, far better than the separated components CNNS and $\text{NH}_4\text{V}_4\text{O}_{10}$. Moreover, it is effective for the wide concentration range from 5 to $40 \text{ mg}\cdot\text{L}^{-1}$ of CIP, inferring a prospect of practical application. The excellent reusability has also been confirmed by a still maintained photo-degradation efficiency of 96.5% and changeless structure for 50-CNNS/ $\text{NH}_4\text{V}_4\text{O}_{10}$ after the five recycle tests. The mechanism investigation indicates excellent activity and stability can be attributed to the formation of the interlaminar 2D/2D S-type heterojunctions which has the merits of the more effective interface contact, suitable pore structure, favorable charge transport paths and the abundant active sites. The matched energy levels will not only accelerate the separation and transfer of photogenerated e^- - h^+ pairs, but also keep the higher redox potential, all well promoting the photocatalytic removal efficiency. In addition, the bigger surface area and special surface NH_4^+ groups will significantly enhance the adsorption capacity toward CIP. This work provided a new idea to develop a kind of multifunctional intercalated 2D ammonium metavanadate materials by *in situ* assembled strategy, which will be especially potential in the application to remove the fluorine-contained contaminant in the actual wastewater.

CRediT authorship contribution statement

Wang Xiaojing: Conceptualization, Funding acquisition, Project administration, Resources, Supervision, Writing – review & editing. **Le Shukun:** Funding acquisition, Methodology, Project administration, Supervision. **Liu Quansheng:** Data curation, Investigation. **He Dan:** Investigation, Methodology, Validation. **Ma Yuxuan:** Conceptualization, Investigation, Methodology, Writing – original draft.

Declaration of Competing Interest

The authors declare that they have no known competing financial interests or personal relationships that could have appeared to influence the work reported in this paper.

Data Availability

The authors do not have permission to share data.

Acknowledgments

The authors are grateful to the financial supports from the National Natural Science Foundation of China (Grants 22062016), the Major Project of Inner Mongolia Natural Science Foundation (Grants 2020ZD02), the Project of Inner Mongolia Natural Science Foundation (Grants 2021BS02016), the Project of the Key Science and Technology of Inner Mongolia of China (Grants 2020GG0135), the Grassland Talent Innovation Team of Inner Mongolia Region (12000-12102619) and Basic Scientific Research Expenses Program of Universities directly under Inner Mongolia Autonomous Region (JY20220286). The authors also would like to thank Shiyanjia Lab (www.shiyanjia.com) for the help of testing.

Appendix A. Supporting information

Supplementary data associated with this article can be found in the online version at [doi:10.1016/j.apcatb.2023.123642](https://doi.org/10.1016/j.apcatb.2023.123642).

References

- [1] J. Du, H. Zhao, S. Liu, H. Xie, Y. Wang, J. Chen, Antibiotics in the coastal water of the South Yellow Sea in China: Occurrence, distribution and ecological risks, *Sci. Total Environ.* 595 (2017) 521–527.
- [2] S. Sun, H. Guo, Q. Ke, J. Sun, S. Shi, M. Zhang, Q. Zhou, Degradation of antibiotic ciprofloxacin hydrochloride by photo-fenton oxidation process, *Environ. Eng. Sci.* 26 (2009) 753–759.
- [3] Y. Deng, L. Tang, C. Feng, etc. construction of plasmonic Ag modified phosphorous-doped ultrathin g-C₃N₄ nanosheets/BiVO₄ photocatalyst with enhanced visible-near-infrared response ability for ciprofloxacin degradation, *J. Hazard. Mater.* 344 (2018) 758–769.
- [4] G. Divyapriya, J. Mohanalakshmi, I.M. Nambi, Electro-enhanced adsorptive removal of ciprofloxacin from aqueous solution on graphite felt, *J. Environ. Chem. Eng.* 8 (2020), 104299.
- [5] A.A. Ghani, A. Shahzad, M. Mozahida, K. Tahir, H. Jeon, B. Kim, D.S. Lee, Adsorption and electrochemical regeneration of intercalated Ti₃C₂Tx MXene for the removal of ciprofloxacin from wastewater, *Chem. Eng. J.* 421 (2021), 127780.
- [6] X. Wang, Y. Wang, C. Zhao, Y. Zhu, Z. Sun, H.J.S. Fan, H. Zheng, Ciprofloxacin removal by ultrasound-enhanced carbon nanotubes/permanganate process: In situ generation of free reactive manganese species via electron transfer, *Water Res* 202 (2021), 117393.

[7] Q. Chen, Q. Xia, Y. Xu, P. Wang, Q. Tan, $\text{NH}_4\text{V}_4\text{O}_{10}$ micro-flowers as cathode material for high performance hybrid magnesium-lithium-ion batteries, *Mater. Lett.* 247 (2019) 178–181.

[8] Y. Lin, J. Li, P. Ren, X. Yang, $\text{NH}_4\text{V}_4\text{O}_{10}$ nanobelts vertically grown on 3D tin nanotube arrays as high-performance electrode materials of supercapacitors, *RSC Adv.* 11 (2021) 8468–8474.

[9] T.N. Vo, H. Kim, J. Hur, W. Choi, I.T. Kim, Surfactant-assisted ammonium vanadium oxide as a superior cathode for calcium-ion batteries, *J. Mater. Chem. A* 6 (2018) 22645–22654.

[10] G.S. Zakhrova, I.V. Baklanova, A.Y. Suntsov, Y. Liu, Q. Zhu, W. Chen, $\text{NH}_4\text{V}_3\text{O}_7$: Synthesis, morphology, and optical properties, *Russ. J. Inorg. Chem.* 61 (2016) 1584–1590.

[11] D. Kundu, B.D. Adams, V. Duffort, S.H. Vajargah, L.F. Nazar, A high-capacity and long-life aqueous rechargeable zinc battery using a metal oxide intercalation cathode, *Nat. Energy* 1 (2016) 1–8.

[12] Y. Zheng, Y. Jiao, Y. Zhu, Q. Cai, A. Vasileff, H.L. Lu, Y. Han, Y. Chen, S.Z. Qiao, Molecule-level $\text{g-C}_3\text{N}_4$ coordinated transition metals as a new class of electrocatalysts for oxygen electrode reactions, *J. Am. Chem. Soc.* 139 (2017) 3336–3339.

[13] J. Fu, J. Yu, C. Jiang, B. Cheng, W. You, J. Yu, Hierarchical porous O-doped $\text{g-C}_3\text{N}_4$ with enhanced photocatalytic CO_2 reduction activity, *Small* 13 (2017), 1603938.

[14] Y. Zhang, Y. Li, Y. Yuan, K. Lin, C-dots decorated $\text{SrTiO}_3/\text{NH}_4\text{V}_4\text{O}_{10}$ Z-scheme heterojunction for sustainable antibiotics removal: Reaction kinetics, DFT calculation and mechanism insight, *Sep Purif. Technol.* 295 (2022), 121268.

[15] S. Majumder, N. Quang, C. Kim, D. Kim, Anion exchange and successive ionic layer adsorption and reaction-assisted coating of BiVO_4 with Bi_2S_3 to produce nanostructured photoanode for enhanced photoelectrochemical water splitting, *J. Colloid Interf. Sci.* 585 (2021) 72–84.

[16] J. Wang, T. Zhou, Y. Zhang, L. Li, C. Zhou, J. Bai, J. Li, H. Zhu, B. Zhou, Type-II Heterojunction $\text{CdIn}_2\text{S}_4/\text{BiVO}_4$ Coupling with CQDs to Improve PEC Water Splitting Performance Synergistically, *ACS Appl. Mater. Inter* 14 (2022) 45392–45402.

[17] H. Yu, L. Shang, T. Bian, S. Run, I. Geoffrey, Nitrogen-doped porous carbon nanosheets templated from $\text{g-C}_3\text{N}_4$ as metal-free electrocatalysts for efficient oxygen reduction reaction, *Adv. Mater.* 28 (2016) 5080–5086.

[18] J. Fu, J. Yu, C. Jiang, C. Bei, $\text{G-C}_3\text{N}_4$ -Based heterostructured photocatalysts, *Adv. Energy Mater.* 8 (2018), 1701503.

[19] C. Prasad, N. Madkhali, V. Govinda, H. Choi, I. Bahadur, S. Sangaraju, Recent progress on the development of $\text{g-C}_3\text{N}_4$ based composite material and their photocatalytic application of CO_2 reductions, *J. Environ. Chem. Eng.* 11 (2023), 109727.

[20] X. Wei, X. Wang, Y. Pu, Facile ball-milling synthesis of $\text{CeO}_2/\text{g-C}_3\text{N}_4$ Z-scheme heterojunction for synergistic adsorption and photodegradation of methylene blue: Characteristics, kinetics, models, and mechanisms, *Chem. Eng. J.* 420 (2021), 127719.

[21] H. Zhao, G. Li, F. Tian, Q. Jia, Y. Liu, R. Chen, $\text{g-C}_3\text{N}_4$ surface-decorated $\text{Bi}_2\text{O}_2\text{CO}_3$ for improved photocatalytic performance: Theoretical calculation and photodegradation of antibiotics in actual water matrix, *Chem. Eng. J.* 366 (2019) 468–479.

[22] N. Pourshirband, A. Nezamzadeh-Ejhieh, S.N. Mirsattari, The $\text{CdS}/\text{g-C}_3\text{N}_4$ nano-photocatalyst: Brief characterization and kinetic study of photodegradation and mineralization of methyl orange, *Spectrochim. Acta A Mol. Biomol. Spectrosc.* 248 (2021), 119110.

[23] B. Zhang, H. Shi, Y. Yan, C. Liu, X. Hu, E. Liu, J. Fan, A novel S-scheme 1D/2D $\text{Bi}_2\text{S}_3/\text{g-C}_3\text{N}_4$ heterojunctions with enhanced H_2 evolution activity, *Colloid Surf. A* 608 (2021), 125598.

[24] X. Yuan, S. Qu, X. Huang, X. Xue, C. Yuan, S. Wang, L. Wei, P. Cai, Design of core-shell $\text{g-C}_3\text{N}_4@ZIF-8$ photocatalyst with enhanced tetracycline adsorption for boosting photocatalytic degradation, *Chem. Eng. J.* 416 (2021), 129148.

[25] H. Jing, R. Ou, H. Yu, Y. Zhao, Y. Lu, M. Huo, H. Huo, X. Wang, Engineering of $\text{g-C}_3\text{N}_4$ nanoparticles/ WO_3 hollow microspheres photocatalyst with Z-scheme heterostructure for boosting tetracycline hydrochloride degradation, *Sep. Purif. Technol.* 255 (2021), 117646.

[26] J. Liu, B. Cheng, J. Yu, A new understanding of the photocatalytic mechanism of the direct Z-scheme $\text{g-C}_3\text{N}_4/\text{TiO}_2$ heterostructure, *Phys. Chem. Chem. Phys.* 18 (2016) 31175.

[27] Y. Xu, G. Fan, P. Sun, Y. Guo, Y. Wang, X. Gu, L. Wu, L. Yu, Carbon nitride pillared vanadate via chemical pre-intercalation towards high-performance aqueous zinc-ion batteries, *Angew. Chem. Int. Ed.* 62 (2023), e202303529.

[28] S. Le, Y. Ma, D. He, X. Wang, Y. Guo, $\text{CdS}/\text{NH}_4\text{V}_4\text{O}_{10}$ S-scheme photocatalyst for sustainable photo-decomposition of amoxicillin, *Chem. Eng. J.* 426 (2021), 130354.

[29] P. Xia, B. Zhu, B. Cheng, J. Yu, J. Xu, 2D/2D $\text{g-C}_3\text{N}_4/\text{MnO}_2$ nanocomposite as a direct Z-scheme photocatalyst for enhanced photocatalytic activity, *ACS Sustain. Chem. Eng.* 6 (2018) 965–973.

[30] B. Lin, H. Li, H. An, W. Hao, J. Wei, Preparation of 2D/2D $\text{g-C}_3\text{N}_4$ nanosheet@ ZnIn_2S_4 nanoleaf heterojunctions with well-designed high-speed charge transfer nanochannels towards high-efficiency photocatalytic hydrogen evolution, *Appl. Catal. B: Environ.* 220 (2018) 542–552.

[31] J. Ran, W. Guo, H. Wang, B. Zhu, S.Z. Qiao, Metal-free 2D/2D phosphorene/ $\text{g-C}_3\text{N}_4$ Van der Waals heterojunction for highly enhanced visible-light photocatalytic H_2 production, *Adv. Mater.* 30 (2018), 1800128.

[32] J. Zou, S. Wu, Y. Liu, Y. Sun, Y. Cao, An ultra-sensitive electrochemical sensor based on 2D $\text{g-C}_3\text{N}_4/\text{CuO}$ nanocomposites for dopamine detection, *Carbon* 130 (2018) 652–663.

[33] Y. Liu, H. Zhang, J. Ke, J. Zhang, W. Tian, X. Xu, X. Duan, H. Sun, M.O. Tade, S. Wang, OD (MoS_2)/2D ($\text{g-C}_3\text{N}_4$) heterojunctions in Z-scheme for enhanced photocatalytic and electrochemical hydrogen evolution, *Appl. Catal. B: Environ.* 228 (2018) 64–74.

[34] D. Batyrbekuly, S. Cajoly, B. Laik, J.P. Pereira-Ramos, N. Emery, Z. Bakenov, R. Baddour-Hadjean, Mechanistic investigation of a hybrid $\text{Zn}/\text{V}_2\text{O}_5$ rechargeable battery with a binary $\text{Li}^+/\text{Zn}^{2+}$ aqueous electrolyte, *ChemSusChem* 13 (2020) 724–731.

[35] D. Huang, Z. Li, G. Zeng, C. Zhou, W. Xue, X. Gong, X. Yan, S. Chen, W. Wang, M. Cheng, Megamerger in photocatalytic field: 2D $\text{g-C}_3\text{N}_4$ nanosheets serve as support of OD nanomaterials for improving photocatalytic performance, *Appl. Catal. B: Environ.* 240 (2019) 153–173.

[36] Y. W, Y. Zhu, Y. Jiang, Photocatalytic self-cleaning carbon nitride nanotube intercalated reduced graphene oxide membranes for enhanced water purification, *Chem. Eng. J.* 356 (2019) 915–925.

[37] Y. Xu, G. Fan, P. Sun, Y. Guo, Y. Wang, X. Gu, L. Wu, L. Yu, Carbon Nitride Pillared Vanadate Via Chemical Pre-Intercalation Towards High-Performance Aqueous Zinc-Ion Batteries, *Angew. Chem. Int. Ed.* 62 (2023), 202303529.

[38] H. Yan, Z. Zhu, Y. Long, W. Li, In-situ intercalation of MoO_{3-x} in $\text{g-C}_3\text{N}_4$ for the enhancement of photocatalytic and antibacterial activities, *J. Photo Photo A* 390 (2020), 112297.

[39] A. Kumar, A. Kumar, G. Sharma, A.H. Al-Muhtaseb, M. Naushad, A.A. Ghifar, C. Guo, F.J. Stadler, Biochar-templated $\text{g-C}_3\text{N}_4/\text{Bi}_2\text{O}_2\text{CO}_3/\text{CoFe}_2\text{O}_4$ nano assembly for visible and solar assisted photo-degradation of paraquat, nitro phenol reduction and CO_2 conversion, *Chem. Eng. J.* 339 (2018) 393–410.

[40] S. Zhong, H. Zhou, M. Shen, et al., Rationally designed a $\text{g-C}_3\text{N}_4/\text{BiO}/\text{Bi}_2\text{O}_2\text{CO}_3$ composite with promoted photocatalytic activity, *J. Alloy. Compd.* 853 (2021), 157307.

[41] J. Zhang, J. Fu, Z. Wang, B. Cheng, K. Dai, W. Ho, Direct Z-scheme porous $\text{g-C}_3\text{N}_4/\text{BiO}$ heterojunction for enhanced visible-light photocatalytic activity, *J. Alloy. Compd.* 766 (2018) 841–850.

[42] S. Sarkar, P.S. Veluri, S. Mitra, Morphology controlled synthesis of layered $\text{NH}_4\text{V}_4\text{O}_{10}$ and the impact of binder on stable high rate electrochemical performance, *Electrochim. Acta* 132 (2014) 448–456.

[43] H. Abbood, H. Peng, X. Gao, B. Tan, K. Huang, Fabrication of cross-like $\text{NH}_4\text{V}_4\text{O}_{10}$ nanobelt array controlled by CMC as soft template and photocatalytic activity of its calcinated product, *Chem. Eng. J.* 209 (2012) 245–254.

[44] J. Jin, Q. Liang, C. Ding, Z. Li, S. Xu, Simultaneous synthesis-immobilization of Ag nanoparticles functionalized 2D $\text{g-C}_3\text{N}_4$ nanosheets with improved photocatalytic activity, *J. Alloy. Compd.* 691 (2017) 763–771.

[45] Y. Bai, W. Mao, Y. Wu, Y. Wu, Y. Gao, T. Wang, S. Liu, Synthesis of novel ternary heterojunctions via Bi_2WO_6 coupling with CuS and $\text{g-C}_3\text{N}_4$ for the highly efficient visible-light photodegradation of ciprofloxacin in wastewater, *Colloid Surf. A* 610 (2021), 125481.

[46] H. Alshaikh, L.A. Al-Hajji, M. Mahmoud, A. Ismail, Visible-light-driven S-scheme mesoporous $\text{Ag}_3\text{VO}_4/\text{g-C}_3\text{N}_4$ heterojunction with promoted photocatalytic performances, *Sep. Purif. Technol.* 272 (2021), 118914.

[47] Y. Zhang, Y. Li, Y. Yuan, K. Lin, C-dots decorated $\text{SrTiO}_3/\text{NH}_4\text{V}_4\text{O}_{10}$ Z-scheme heterojunction for sustainable antibiotics removal: Reaction kinetics, DFT calculation and mechanism insight, *Sep. Purif. Technol.* 295 (2022), 121268.

[48] T.N. Vo, H. Kim, J. Hur, W. Choi, I.T. Kim, Surfactant-assisted ammonium vanadium oxide as a superior cathode for calcium-ion batteries, *J. Mater. Chem. A* 6 (2018) 22645–22654.

[49] L. Jiang, X. Yuan, G. Zeng, Z. Wu, L. Jie, Metal-free efficient photocatalyst for stable visible-light photocatalytic degradation of refractory pollutant, *Appl. Catal. B: Environ.* 221 (2018) 715–725.

[50] L. Liu, L. Ding, Y. Liu, W. An, S. Lin, Y. Liang, W. Cui, A stable $\text{Ag}_3\text{PO}_4@\text{PANI}$ core@shell hybrid: Enrichment photocatalytic degradation with $\pi-\pi$ conjugation, *Appl. Catal. B: Environ.* 201 (2017) 92–104.

[51] D. Wang, F. Jia, H. Wang, C. Fei, X. Yuan, Simultaneously efficient adsorption and photocatalytic degradation of tetracycline by Fe-based MOFs, *J. Colloid Interf. Sci.* 519 (2018) 273–284.

[52] S. Ma, D. Chen a, Y. Zhong, Y. Feng, Z. He, W. Zhang, Y. Zhang, H. Ding, X. Wu, Oxygen vacancy simultaneously inducing peroxymonosulfate activation and photocatalytic reaction for highly efficient ciprofloxacin degradation, *Chem. Eng. J.* 467 (2023), 143385.

[53] Y.T. Zhu, J.J. Xu, M.D. Chen, Synthesis of $\text{La}_2\text{Ti}_2\text{O}_7/\text{Bi}_5\text{O}_7$ photocatalysts with improved photocatalytic activity for degradation of CIP under visible light, *Sep. Purif. Technol.* 282 (2022) 11.

[54] C. Zhao, Y. Li, H.Y. Chu, X. Pan, L. Ling, P. Wang, H.F. Fu, C.C. Wang, Z.H. Wang, Construction of direct Z-scheme $\text{Bi}_5\text{O}_7/\text{UiO}-66-\text{NH}_2$ heterojunction photocatalysts for enhanced degradation of ciprofloxacin: Mechanism insight, pathway analysis and toxicity evaluation, *J. Hazard. Mater.* 419 (2021) 17.

[55] E.B. Simsek, Solvothermal synthesized boron doped TiO_2 catalysts: photocatalytic degradation of endocrine disrupting compounds and pharmaceuticals under visible light irradiation, *Appl. Catal. B: Environ.* 200 (2017) 309–322.

[56] N.R. Khalid, A. Majid, M.B. Tahir, N.A. Niaz, S. Khalid, Carbonaceous-TiO₂ nanomaterials for photocatalytic degradation of pollutants: A review, *Ceram. Int.* 43 (2017) 14552–14571.

[57] L.V. Trandafilović, D.J. Jovanović, X. Zhang, Ptasinska, D.M. Dramicanin, Enhanced photocatalytic degradation of methylene blue and methyl orange by ZnO/Eu nanoparticles, *Appl. Catal. B: Environ.* 203 (2017) 740–752.

[58] S. Bacha, S. Saitzek, E. McCabe, H. Kabour, Photocatalytic and Photocurrent Responses to Visible Light of the Lone-Pair-Based Oxsulfide $\text{Sr}_6\text{Cd}_2\text{Sb}_6\text{S}_10\text{O}_7$, *Inorg. Chem.* 61 (2022) 18611–18621.

[59] B. Chai, J. Yan, C. Wang, Z. Ren, Y. Zhu, Enhanced visible light photocatalytic degradation of Rhodamine B over phosphorus doped graphitic carbon nitride, *Appl. Surf. Sci.* 391 (2017) 376–383.

[60] S. Dong, X. Ding, T. Guo, X. Yue, X. Han, J. Sun, Self-assembled hollow sphere shaped Bi₂WO₆/RGO composites for efficient sunlight-driven photocatalytic degradation of organic pollutants, *Chem. Eng. J.* 316 (2017) 778–789.

[61] P. Xia, S. Cao, B. Zhu, M. Liu, M. Shi, J. Yu, Y. Zhang, Designing a 0D/2D S-Scheme Heterojunction over Polymeric Carbon Nitride for Visible-Light Photocatalytic Inactivation of Bacteria, *Angew. Chem., Int. Ed.* 59 (2020) 5218–5225.

[62] P. Li, J. Guo, X. Ji, Y. Xiong, Q. Lai, S. Yao, Y. Zhu, Y. Zhang, P. Xiao, Construction of direct Z-scheme photocatalyst by the interfacial interaction of WO₃ and SiC to enhance the redox activity of electrons and holes, *Chemosphere* 282 (2021), 130866.

[63] H. Dong, X. Guo, C. Yang, Z. Ouyang, Synthesis of g-C₃N₄ by different precursors under burning explosion effect and its photocatalytic degradation for tylosin, *Appl. Catal. B: Environ.* 230 (2018) 65–76.

[64] Y. Ma, D. He, X. Wang, Y. Fu, A thin clothe coated architecture of ZnIn₂S₄/H₂Ta₂O₆ for enhanced photocatalytic hydrogen production, *Int. J. Hydrol. Energ.* 46 (2021) 38701–38711.

[65] S.G. Kumar, K.S.R.K. Rao, Comparison of modification strategies towards enhanced charge carrier separation and photocatalytic degradation activity of metal oxide semiconductors (TiO₂, WO₃ and ZnO), *Appl. Surf. Sci.* 391 (2017) 124–148.

[66] X.J. Wen, C.G. Niu, L. Zhang, C. Liang, H. Guo, G.M. Zeng, Photocatalytic degradation of ciprofloxacin by a novel Z-scheme CeO₂-Ag/AgBr photocatalyst: Influencing factors, possible degradation pathways, and mechanism insight, *J. Catal.* 358 (2018) 141–154.

[67] J. Sha, L. Li, Z. An, M. He, H. Yu, Y. Wang, B. Gao, S. Xu, Diametrically opposite effect of Cu²⁺ on sulfamerazine and ciprofloxacin adsorption-photodegradation in g-C₃N₄/visible light system: behavior and mechanism study, *Chem. Eng. J.* 428 (2022), 131065.

[68] H.M. Heise, R. Kurte, Fourier-transform infrared spectroscopy for quantification of hydrogen fluoride in sulfur hexafluoride decomposed by partial discharges and sparks, *J. Mol. Struct.* 653 (2003) 555–559.